Dalton Transactions

PAPER

View Article Online
View Journal | View Issue

Cite this: *Dalton Trans.*, 2015, **44**, 3109

Structural, transport and optical properties of $(La_{0.6}Pr_{0.4})_{0.65}Ca_{0.35}MnO_3$ nanocrystals: a wide band-gap magnetic semiconductor

Satyam Kumar,[a] G. D. Dwivedi,[b] Shiv Kumar,[a] R. B. Mathur,[c] U. Saxena,[d] A. K. Ghosh,[a] Amish G. Joshi,[c] H. D. Yang[b] and Sandip Chatterjee*[e]

Received 11th November 2014,
Accepted 11th December 2014

DOI: 10.1039/c4dt03452j

www.rsc.org/dalton

$(La_{0.6}Pr_{0.4})_{0.65}Ca_{0.35}MnO_3$ system has been synthesized *via* a sol–gel route at different sintering temperatures. Structural, transport and optical measurements have been carried out to investigate $(La_{0.6}Pr_{0.4})_{0.65}Ca_{0.35}MnO_3$ nanoparticles. Raman spectra show that Jahn–Teller distortion has been decreased due to the presence of Ca and Pr in A-site. Magnetic measurements provide a Curie temperature around 200 K and saturation magnetization (M_S) of about 3.43μ_B/Mn at 5 K. X-ray photoemission spectroscopy study suggests that Mn exists in a dual oxidation state (Mn^{3+} and Mn^{4+}). Resistivity measurements suggest that charge-ordered states of Mn^{3+} and Mn^{4+}, which might be influenced by the presence of Pr, have enhanced insulating behavior in $(La_{0.6}Pr_{0.4})_{0.65}Ca_{0.35}MnO_3$. Band gap estimated from UV-Vis spectroscopy measurements comes in the range of wide band gap semiconductors (~3.5 eV); this makes $(La_{0.6}Pr_{0.4})_{0.65}Ca_{0.35}MnO_3$ a potential candidate for device application.

Introduction

Hole doped manganite systems have been generating curiosity among scientists and engineers for more than 60 years because of their unprecedented and wide range of properties, *e.g.*, ferromagnetism, insulator-metal transition and colossal magnetoresistive properties. The physics behind all these properties is even more challenging and has attracted attentions of theoreticians and experimentalists with almost equal authority.[1–11] Manganite materials have been used in different electronic devices such as magneto-tunable photocurrent devices, resistive switching devices, and spin hall magnetoresistive devices.[12–18] The parent compound $LaMnO_3$ is known to be an antiferromagnetic insulator, while divalent cation (Ca^{2+}, Sr^{2+} and Ba^{2+}) doping induces paramagnetism with polaron type conductivity at high temperatures, and metallic ferromagnetism below the Curie temperature T_C. The origin of ferromagnetism has been attributed to the double-exchange interaction between the valence electronic states of Mn^{3+}–O^{-2}–Mn^{4+}.[19–21] The double-exchange mechanism along with the effect of lattice distortion is believed to be responsible for the occurrence of colossal magnetoresistance (CMR).[22,23] As an outcome of the double-exchange interaction and the lattice distortion, a large spin splitting of the conduction band (majority and minority sub-bands) takes place in the ferromagnetic state.[8–11] Governed by the Hund's rule, these sub-bands are separated by few electron-volts energy, which depends on A-site doping. The large spin splitting produces the half-metallic properties of the material because at Fermi level, charge carriers with only one spin direction (up/down) are present, whereas there is a gap in the density of states for the carriers with the other spin direction (down/up).

Hole doped manganite systems in the nano-range act in a different way, *i.e.*, ferromagnetic ordering and metal-insulator transition are well separated from each other. Transport properties basically depend on boundary conditions. In nano-range, surface to volume ratio increases; thus, the boundary effect becomes more pronounced in transport properties. Due to more boundaries, charge carriers face much more scattering, and as a result the resistivity of the system increases. However, the double exchange interaction between Mn^{3+} and Mn^{4+} is not affected by the boundary conditions, and therefore it is not affected much in the nano-phase.[24]

Magnetic properties of Ca doped $PrMnO_3$ ($Pr_{1-x}Ca_xMnO_3$) materials at low temperatures are governed by Mn^{3+}/Mn^{4+} ordering, intra- and inter-Mn exchange interactions and structural distortions produced by the Ca^{2+} cations. $PrMnO_3$ has an antiferromagnetic ground state. With Ca doping, a ferromagnetic ground state develops for x = 0.2. The charge-ordering of the Mn-ions occurs over a wide range from 0.3 < x < 0.75 with an

[a]*Department of Physics, Banaras Hindu University, Varanasi-221005, India*
[b]*Department of Physics, National Sun Yat-sen University, Kaohsiung-80424, Taiwan*
[c]*CSIR-National Physical Laboratory, Dr. K.S. Krishnan Road, New Delhi-110012, India*
[d]*Department of Physics, Mahila Mahavidyalaya, Banaras Hindu University, Varanasi-221005, India*
[e]*Department of Physics, Indian Institute of Technology (Banaras Hindu University), Varanasi-221005, India. E-mail: schatterji.app@iitbhu.ac.in*

ordering temperature near 250 K.[25,26] $Pr_{0.65}Ca_{0.35}MnO_3$ shows insulating behavior in both the paramagnetic and ferromagnetic states because of the charge-ordered state of Mn^{3+} and Mn^{4+}.[27]

Magnetic and transport properties of manganites have been studied with great interest and enthusiasm by scientists and will be continued to be studied in the future because of the vast range of properties these systems possess which make them desirable from an application point of view. However, studies have not been done concerning their optical properties because these systems show either insulator (large band gap; typically >4 eV) behavior or metallic (no band gap) behavior, which makes them less interesting for optical studies. In this manuscript, we have doped 40% Pr in the La site of $La_{0.65}Ca_{0.35}MnO_3$ system, which shows metallic ferromagnetic behavior below 260 K.[28] The idea behind the doping of Pr is that the $Pr_{0.65}Ca_{0.35}MnO_3$ system shows ferromagnetic charge-ordered insulator behavior. We are expecting that with the doping of Pr, the semiconducting behavior will increase because of the stabilization of charge-ordering, along with the sustaining magnetic order of the system. Along with a strong magnetic moment, if we can induce a semiconducting nature, these systems can be used as a better candidate to improve magnetic semiconducting devices. To realize this phenomenon, we have used $La_{0.65}Ca_{0.35}MnO_3$ nanoparticles, which show better semiconducting nature along with ferromagnetic ordering as compared to its bulk counterpart. In addition, the doping of Pr may also increase its semiconducting behavior without disturbing the magnetic ordering. We are using particularly 40% of Pr doping in the La site because excess doping results in a completely insulating phase, while doping less than 40% decreases the band gap significantly,[10] and both the cases are not favorable for application purpose.

Experimental section

$(La_{0.6}Pr_{0.4})_{0.65}Ca_{0.35}MnO_3$ samples were synthesized using the sol–gel method. Analytical grade metal oxides Pr_6O_{11}, La_2O_3, and $CaCO_3$ powders were taken in stoichiometric proportions (0.39 mol: 0.26 mol: 0.35 mol) and dissolved in nitric acid (HNO_3) and thoroughly mixed for 30 minutes. The prepared solution of metal nitrates along with $Mn(NO_3)_3{\cdot}4H_2O$ (1 mol) were mixed in aqueous solution of citric acid [$C_6H_8O_7$] (99.5% purity) with stirring, to obtain a homogeneous precursor solution. Citric acid serves as the fuel for the reaction. In this solution, ethylene glycol was added drop wise with stirring. Citric acid, ethylene glycol and metal nitrates were precisely taken in a 4 : 3 : 1 molar ratio. The precursor solution was dried at 200 °C for 12 h in an oven to obtain xerogel and the swelled xerogel was kept at 300 °C for 5 h to dry. After grinding the xerogel, powders were sintered at 600, 800, 1000 °C for 5 h under air to obtain $(La_{0.6}Pr_{0.4})_{0.65}Ca_{0.35}MnO_3$ nanoparticles.

Phase purity of the as-prepared $(La_{0.6}Pr_{0.4})_{0.65}Ca_{0.35}MnO_3$ samples were checked with a Model: Philips X'pert ProX-ray diffractometer using CuK_α radiation (λ = 1.5406 Å). Transmission electron microscopy measurements were done with a JEOL-2010 (Japan). Raman spectra were obtained with a Renishaw micro-Raman spectroscope in the range of 100 cm^{-1}–1000 cm^{-1} using 514.5 nm Ar^+ laser as the excitation source. Fourier transform infrared (FTIR) spectroscopy measurements were done with an FTIR Spectrometer (Spectrum One, Perkin Elmer Instrument, USA) in the range of 4000–400 cm^{-1} with a resolution of 1 cm^{-1}. Magnetic measurements were done using a superconducting quantum interference device [Magnetic Property Measurement System (MPMS) XL-7, Quantum Design Inc.]. Room temperature X-ray photoemission spectroscopy measurements were done using a Omicron multiprobe surface analysis system operating at an average base pressure of ~5×10^{-10} torr with a monochromatic AlK_α line at 1486.70 eV. The total energy resolution, estimated from the width of the Fermi edge, was about 0.25 eV for monochromatic AlK_α line with photon energy 1486.70 eV. Resistivity measurements were done *via* 2-probe method using a Keithley 2400 Source meter. The optical absorption spectra were measured in the range of 220–800 nm using a UV-Vis spectrometer (SHIMADZU).

Results and discussion

Structural analysis

X-ray diffraction patterns of $(La_{0.6}Pr_{0.4})_{0.65}Ca_{0.35}MnO_3$ sintered at 600 °C, 800 °C and 1000 °C have been shown in Fig. 1. All the three samples are in single phase (without any secondary phase) and crystallize in orthorhombic *Pbnm* space group like their extreme parents $La_{0.65}Ca_{0.35}MnO_3$ and $Pr_{0.65}Ca_{0.35}MnO_3$. We have determined average crystallite size (D) of all the three samples sintered at 600 °C, 800 °C and 1000 °C from the Scherrer's formula:

$$D = \frac{0.9\lambda}{\beta \cos \theta}$$

where λ = 1.5406 Å, wavelength of X-ray used, β is full width at half maximum (FWHM) of Bragg's reflection plane and θ is

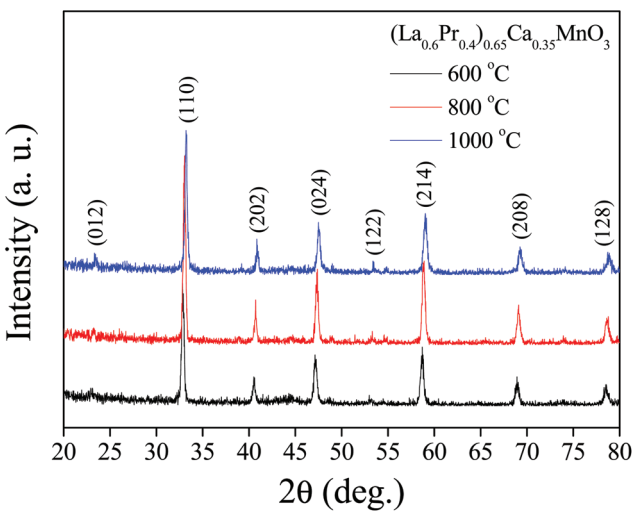

Fig. 1 X-ray diffraction pattern of $(La_{0.6}Pr_{0.4})_{0.65}Ca_{0.35}MnO_3$ nanoparticles sintered at 600 °C, 800 °C and 1000 °C.

Table 1 Particle sizes estimated from X-ray diffraction and TEM, and average strain estimated using Williamson–Hall method

Samples	Average strain (estimated using Williamson–Hall method)	Particle size (nm) (estimated from XRD data)	Particle size (nm) (estimated from TEM)
$(La_{0.6}Pr_{0.4})_{0.65}Ca_{0.35}MnO_3$ sintered at 600 °C	1.58×10^{-3}	25	36
$(La_{0.6}Pr_{0.4})_{0.65}Ca_{0.35}MnO_3$ sintered at 800 °C	2.75×10^{-3}	27	38
$(La_{0.6}Pr_{0.4})_{0.65}Ca_{0.35}MnO_3$ sintered at 1000 °C	4.92×10^{-3}	29	42

half of the angle of the corresponding reflection plane. We have used the most intense peak (110) as a reference plane to calculate the crystallite size, which is observed to be about 25 nm, 27 nm and 29 nm for the samples sintered at 600 °C, 800 °C and 1000 °C, respectively. We have also estimated the strain using the Williamson–Hall method.[29] The average strain values for different sizes of $(La_{0.6}Pr_{0.4})_{0.65}Ca_{0.35}MnO_3$ are given in Table 1.

To study the surface morphology and microstructure of $(La_{0.6}Pr_{0.4})_{0.65}Ca_{0.35}MnO_3$ nanocrystals, low-resolution transmission electron microscopy (TEM) measurements have been performed. Due to the strong magnetic moment, particles are strongly agglomerated with each other to make irregular shapes and sizes, which makes it rather difficult to distinguish one from the other. Estimated average grain sizes of the three samples sintered at 600 °C, 800 °C and 1000 °C is observed to be about 36 nm, 38 nm and 42 nm respectively, which is consistent with the X-ray diffraction results, which suggests increase in crystallite sizes with increasing sintering temperature (Fig. 2(a, c and e)). Selected area electron diffraction (SAED) images show increase in crystalline nature of $(La_{0.6}Pr_{0.4})_{0.65}Ca_{0.35}MnO_3$ system with increase in sintering temperature (Fig. 2(b, d and f)). $(La_{0.6}Pr_{0.4})_{0.65}Ca_{0.35}MnO_3$ sintered at 1000 °C shows much clearer and brighter Bragg's spots than the rest of the two systems sintered at 600 °C and 800 °C, which indicates the better crystalline nature of this system. X-ray diffraction, low-resolution TEM and SAED measurements have confirmed the single crystalline nature of our samples with almost homogeneous distribution.

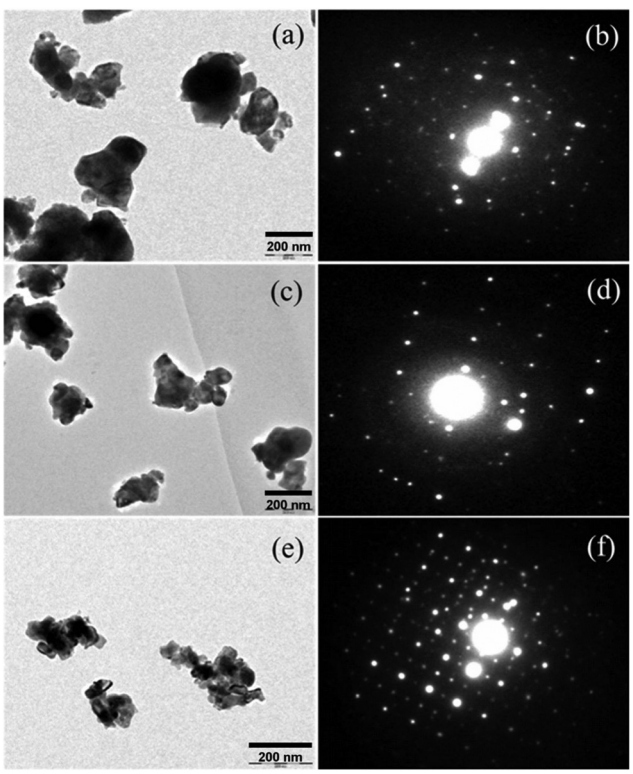

Fig. 2 Low-resolution transmission electron micrographs and their corresponding selected area electron diffraction images of $(La_{0.6}Pr_{0.4})_{0.65}Ca_{0.35}MnO_3$ nanoparticles sintered at 600 °C (a, b), 800 °C (c, d) and 1000 °C (e, f).

Raman spectroscopy

To investigate crystal structure, lattice distortions and defects, Raman spectroscopy is considered to be the most powerful non-destructive technique. We doped 40% Pr in the La-site of $La_{0.65}Ca_{0.35}MnO_3$ to obtain magnetic semiconductor materials. To study the effect of doping on the crystal structure and lattice distortions, we obtained Raman spectra of $(La_{0.6}Pr_{0.4})_{0.65}Ca_{0.35}MnO_3$ nanoparticles sintered at 600 °C, 800 °C and 1000 °C, which have been shown in Fig. 3. In the orthorhombic rare-earth manganites, Raman modes become active due to deviations from the ideal cubic perovskite structure. Group theory analysis of the $LaMnO_3$ structure suggests 60 normal modes. Among all these 60 modes, only 24 modes are Raman active and the remaining modes are infrared (IR) active.[30]

$$\Gamma_{optical} = (7A_g + 7B_{1g} + 5B_{2g} + 5B_{3g})_{Raman} + (8A_u + 10B_{1u} + 8B_{2u} + 10B_{3u})_{IR}$$

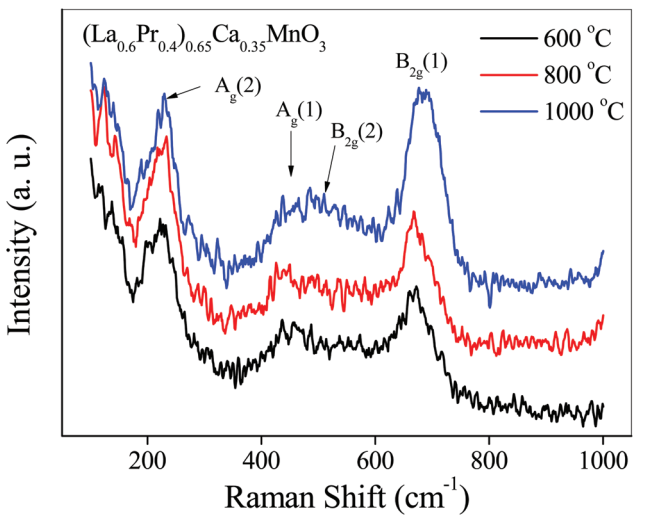

Fig. 3 Raman spectra of $(La_{0.6}Pr_{0.4})_{0.65}Ca_{0.35}MnO_3$ nanoparticles sintered at 600 °C, 800 °C and 1000 °C.

These 24 Raman active modes can be divided into 2 symmetric modes, 4 asymmetric stretching modes, 4 bending modes, 6 rotation/tilt modes of the octahedral, and the remaining 8 modes are associated with the motion of A-site (La/Pr/Ca) cations. All these Raman modes become active because of 4 fundamental distortions from the ideal perovskite structure, namely, rotations of MnO_6 octahedra around the cubic $[001]_c$ and $[110]_c$ axes, Jahn–Teller distortion, and A-site (La/Pr/Ca) shift from its position in the ideal perovskite lattice. The Raman spectra of $(La_{0.6}Pr_{0.4})_{0.65}Ca_{0.35}MnO_3$ sintered at 600 °C, 800 °C and 1000 °C do not show any phase changes due to change in sintering temperature (Fig. 3). We observed 3 distinct Raman modes in 200–800 cm^{-1} range; first, around 230 cm^{-1}, second around 500 cm^{-1} and third around 680 cm^{-1}. The Raman mode around 680 cm^{-1} assigned as $B_{2g}(1)$ is related to the symmetric stretching vibration of oxygen in MnO_6 octahedra. However, a very broad Raman mode around 500 cm^{-1} can be divided into two distinct modes, namely, 460 cm^{-1}($A_g(1)$) and 520 cm^{-1} ($B_{2g}(2)$), related to the Jahn–Teller type asymmetric stretching mode and symmetric bending modes of MnO_6 octahedra, respectively. Dediu *et al.*[31] reported that $Pr_{0.65}Ca_{0.35}MnO_3$ shows no variation in Raman spectra above the charge-ordered transition temperature (T_{CO}), while below T_{CO}, Raman mode near 475 cm^{-1} has been divided into two modes: $A_g(1)$ and $B_{2g}(2)$. In our case, due to the presence of Ca and Pr in A-site, the Jahn–Teller distortion at room temperature further suppressed, and the Raman mode related to this becomes relatively less prominent.[29] Consequently, the modes around 500 cm^{-1} are not considerably distinguishable. The Raman mode around 230 cm^{-1} denoted as $A_g(2)$ is related to the tilting of MnO_6 octahedra. Raman modes observed in the range of 100–200 cm^{-1} are predominantly because of the vibrations of A-site cations.

Fourier transform infrared spectroscopy

To get information about the molecular and functional species present on the surface and to further investigate lattice vibration present in our system, we used Fourier transform infrared (FTIR) spectroscopy. FTIR measurements of $(La_{0.6}Pr_{0.4})_{0.65}Ca_{0.35}MnO_3$ sintered at 600 °C, 800 °C and 1000 °C have been shown in Fig. 4. In the finger-print region, the band around 600 cm^{-1} corresponds to the characteristic Mn–O bond. This confirms that each sample strongly contains Mn–O bond and a change in the bond length of Mn–O–Mn, because of the internal motion, is responsible for the band formation. Stretching vibration is responsible for the change in Mn–O–Mn length, while bending vibration involves the change of Mn–O–Mn bond angle. The peaks at 1400 and 1630 cm^{-1} corresponds to the asymmetric stretching vibrations of C=C bond and symmetric stretching of C=O bond in citrate (which formed in the solution and may be present on the surface of nano-crystals).

Magnetic properties

To investigate the magnetic properties of $(La_{0.6}Pr_{0.4})_{0.65}Ca_{0.35}MnO_3$ nanoparticles sintered at 600 °C, 800 °C and 1000 °C, we performed temperature dependent field cooled magnetization measurements (M–T) from 300 K to 5 K at 100 Oe magnetic field (Fig. 5). M–T measurement of all the samples show that ferromagnetic transition occurs around 200 K and particle size is not showing any significant effect on Curie temperature, but it is considerably affecting the magnetic moment. $(La_{0.6}Pr_{0.4})_{0.65}Ca_{0.35}MnO_3$ sintered at 600 °C, 800 °C and 1000 °C show magnetic moments of 6.58 emu gm^{-1}, 8.56 emu gm^{-1} and 7.53 emu gm^{-1}, respectively, at 5 K. At a low magnetic field, the $(La_{0.6}Pr_{0.4})_{0.65}Ca_{0.35}MnO_3$ sintered at 800 °C shows a higher magnetization value than the $(La_{0.6}Pr_{0.4})_{0.65}Ca_{0.35}MnO_3$ sintered at 1000 °C; however, at a

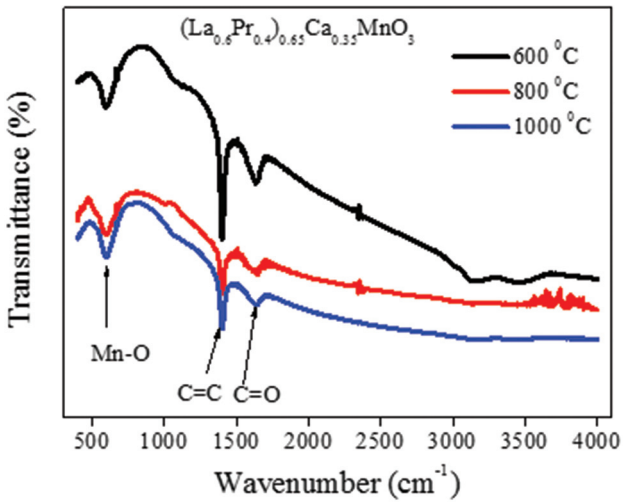

Fig. 4 Fourier transform infrared spectroscopy of $(La_{0.6}Pr_{0.4})_{0.65}Ca_{0.35}MnO_3$ nanoparticles sintered at 600 °C, 800 °C and 1000 °C.

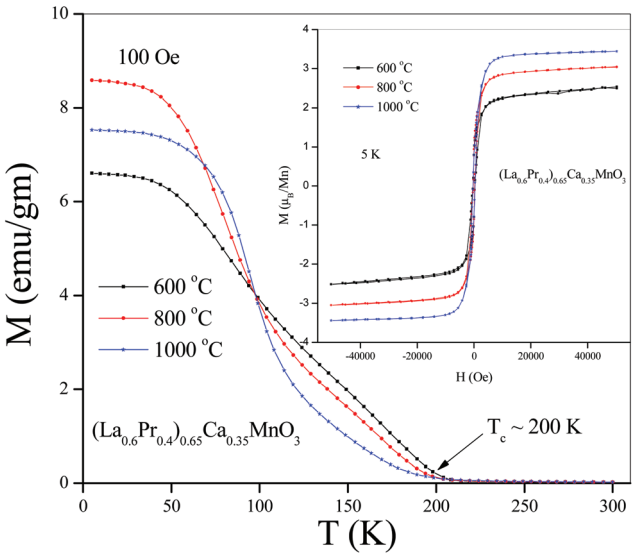

Fig. 5 Field cooled temperature dependent magnetization measurements of $(La_{0.6}Pr_{0.4})_{0.65}Ca_{0.35}MnO_3$ nanoparticles sintered at 600 °C, 800 °C and 1000 °C at 100 Oe magnetic field down to 5 K. Inset figure shows the M–H hysteresis loop up to 5 T magnetic field at 5 K.

higher field $(La_{0.6}Pr_{0.4})_{0.65}Ca_{0.35}MnO_3$ sintered at 1000 °C shows a higher saturated magnetic moment. Calculated saturation magnetization (M_s) of $(La_{0.6}Pr_{0.4})_{0.65}Ca_{0.35}MnO_3$ is observed to be around 3.65μ_B/Mn (with 65% of Mn^{3+} and 35% of Mn^{4+}). *M–H* measurements at 5 K show that 5 T magnetic field gives saturation magnetization of 2.49μ_B/Mn, 3.03μ_B/Mn and 3.43μ_B/Mn for $(La_{0.6}Pr_{0.4})_{0.65}Ca_{0.35}MnO_3$ sintered at 600 °C, 800 °C and 1000 °C, respectively (inset Fig. 5). Magnetic moment observed for $(La_{0.6}Pr_{0.4})_{0.65}Ca_{0.35}MnO_3$ sintered at 1000 °C is very close to the calculated magnetic moment 3.65μ_B/Mn. This shows that with increasing particle size, magnetic response increases consistently and approaches the magnetic moment of bulk $(La_{0.6}Pr_{0.4})_{0.65}Ca_{0.35}MnO_3$. This confirms the strong ferromagnetic character of our samples below 200 K. The ferromagnetic behavior of a similar $(La_{0.7}Pr_{0.3})_{0.65}Ca_{0.35}MnO_3$ has been reported earlier,[32] which is consistent with our result.

X-ray photoemission spectroscopy

X-ray photoemission spectroscopy (XPS) study has been done to investigate the chemical state of $(La_{0.6}Pr_{0.4})_{0.65}Ca_{0.35}MnO_3$ nanoparticles sintered at 600 °C, 800 °C and 1000 °C (Fig. 6). A survey scan of $(La_{0.6}Pr_{0.4})_{0.65}Ca_{0.35}MnO_3$ sintered at 600 °C, 800 °C and 1000 °C confirms the presence of La, Pr, Ca, Mn and O on the surface (Fig. 6(a)). High resolution XPS core level spectra of Ca2p, O1s, and Mn2p regions have been shown in Fig. 6(b), (c) and (d) respectively. In the Ca2p region, peaks observed at 345.5 eV and 349 eV have been denoted as $Ca2p_{3/2}$ and $Ca2p_{1/2}$. The spin–orbit splitting energy is 3.5 eV, which indicates that the Ca exists in +2 oxidation state. In O1s region, two peaks at 528.7 eV and 530.7 eV are attributed to the contribution of the crystal lattice oxygen and adsorbed oxygen, respectively. The adsorbed oxygen has a tendency to bind with oxygen vacancies (V_o). In the Mn2p region, the two

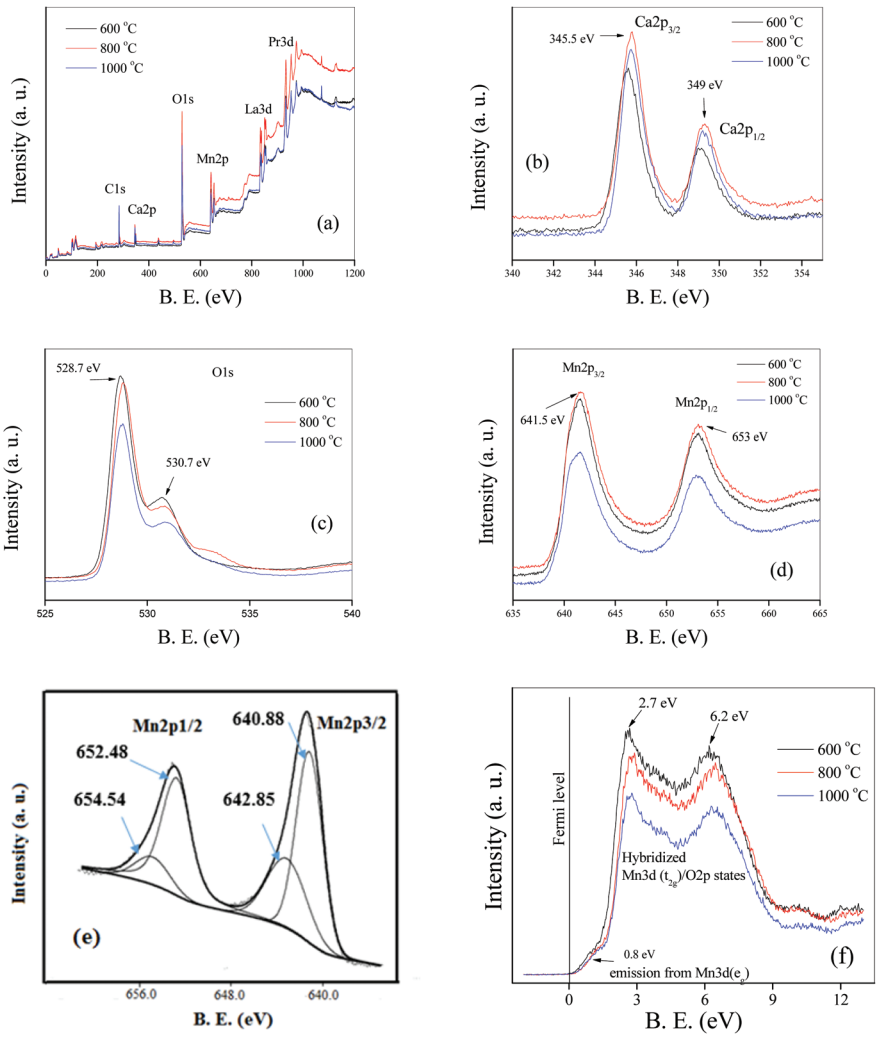

Fig. 6 (a) Survey scan X-ray photoemission spectroscopy (XPS) for $(La_{0.6}Pr_{0.4})_{0.65}Ca_{0.35}MnO_3$ nanoparticles sintered at 600 °C, 800 °C and 1000 °C. High resolution core level XPS of (b) Ca2p region, (c) O1s region, (d) Mn2p region for $(La_{0.6}Pr_{0.4})_{0.65}Ca_{0.35}MnO_3$ nanoparticles sintered at 600 °C, 800 °C and 1000 °C. (e) Deconvoluted peaks of Mn2p region for $(La_{0.6}Pr_{0.4})_{0.65}Ca_{0.35}MnO_3$ nanoparticles sintered at 600 °C as a representative. (f) Valence band spectra of $(La_{0.6}Pr_{0.4})_{0.65}Ca_{0.35}MnO_3$ nanoparticles sintered at 600 °C, 800 °C and 1000 °C.

peaks are located at 641.5 and 653 eV, which belong to $Mn2p_{3/2}$ and $Mn2p_{1/2}$, respectively. The peaks of $Mn2p_{3/2}$ and $Mn2p_{1/2}$ can be deconvoluted into two peaks each. The deconvoluted peaks of Mn2p region for $(La_{0.6}Pr_{0.4})_{0.65}Ca_{0.35}MnO_3$ sintered at 600 °C have been shown as a representative in Fig. 6(e). The deconvoluted peaks of $Mn2p_{3/2}$ at 640.88 eV and 642.85 eV (and $Mn2p_{1/2}$ at 652.48 eV and 654.54 eV) represent Mn^{3+} and Mn^{4+}, respectively. This confirms that Mn exists in two oxidation states (+3 and +4), which participate in the double exchange interaction to give ferromagnetic ordering in the system. Valence band spectra have been shown in Fig. 6(f) for the discussed nanoparticles. The two most intense peaks around 2.7 eV and 6.2 eV are due to the strong hybridization of $Mn3d(t_{2g})$ and O2p states. A weak emission near Fermi level have been detected, which belongs to $Mn3d(e_g)$ states. Similar type of features had been reported earlier in manganite materials,[33,34] which supports our result.

Resistivity measurement

$La_{0.65}Ca_{0.35}MnO_3$ shows insulator-metal transition around 260 K[28] but $Pr_{0.65}Ca_{0.35}MnO_3$ shows charge ordered type insulating behavior at low temperatures.[35] The primary reason behind the formation of charge-ordered state in $Pr_{0.65}Ca_{0.35}MnO_3$ is competition between double exchange and super exchange among the core spins of Mn and the coulombic interaction between the electrons of different orbitals of the same Mn-site.[36,37] Fig. 7 shows the variation of resistivity (ρ) with respect to temperature for $(La_{0.6}Pr_{0.4})_{0.65}Ca_{0.35}MnO_3$ sintered at 600 °C, 800 °C and 1000 °C. The $(La_{0.6}Pr_{0.4})_{0.65}Ca_{0.35}MnO_3$ system shows insulator type behavior at higher temperatures because of the development of charge-ordered states in the nano-crystalline system due to the presence of ample amount of Pr in A-sites and it is playing a dominant role in the transport behavior of the system at higher temperatures; however, at low temperatures, double exchange interaction becomes more dominant and the system starts to behave as a metal. The insulator-metal transition temperature (T_{IM}) and resistivity (ρ) of nanoparticles depend on the sintering temperature of the system and decrease with increase of sintering temperature. In other words, insulator-metal transition temperature depends on the particle size of the nanocrystals. As we have seen in X-ray diffraction analysis and low-resolution transmission electron microscopy analysis, particle size increases with increase in sintering temperature. Due to the increase in particle (grain) size, the effect of grain boundary reduces and consequently the charge carrier faces less scattering from grain boundaries. This factor also improves the double exchange interaction mechanism and the system starts to show metal-insulator transition at higher temperatures, and the resistivity of the system also decreases significantly.

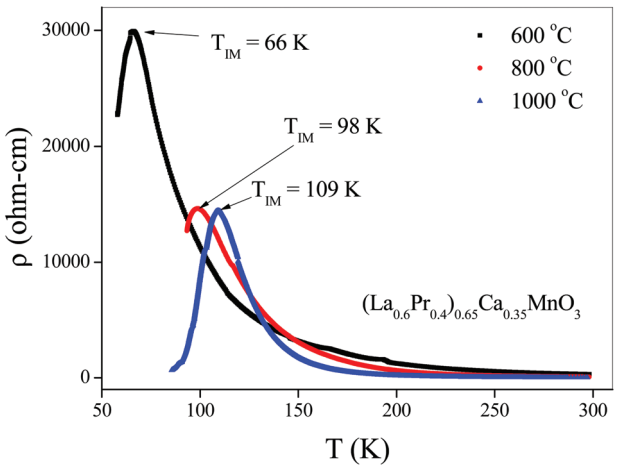

Fig. 7 Variation of resistivity with temperature of $(La_{0.6}Pr_{0.4})_{0.65}Ca_{0.35}MnO_3$ nanoparticles sintered at 600 °C, 800 °C and 1000 °C.

The resistivity of $(La_{0.6}Pr_{0.4})_{0.65}Ca_{0.35}MnO_3$ sintered at 600 °C, 800 °C and 1000 °C can be well fitted by $\rho = \rho_0 \exp(E_a/k_BT)$ for the nearest-neighbour hopping of small polarons (Fig. 8), where k_B is the Boltzmann's constant and E_a is the activation energy. The activation energy (E_a) for the samples was calculated using the small polaron theory, and values are given in Table 2. With increase in sintering temperature, the resistivity decreases and E_a increases. The linear fit shows that thermally activated band conduction is the dominant mechanism in the high-temperature region. The deviation from the linear fit indicates that the thermal activation mechanism is not valid in the low-temperature region. The variable-range-hopping (VRH) conduction of polarons has been found to dominate in this temperature region. The conduction mechanism due to the variable range hopping of polaron at low temperature can be described by the Mott's equation[38–40] $\rho(T) = \rho_0 \exp[T_0/T]^{1/4}$, where ρ_0 and T_0 are constants and are given by $\rho_0 = \{[8\pi\alpha k_B T/N(E_F)]^{1/2}\}/(3e^2\nu_{ph})$ and $T_0 = 18\alpha^3/[k_B N(E_F)]$, where ν_{ph} ($\sim 10^{13}$ s^{-1}) is the phonon frequency at Debye temperature, $N(E_F)$ is the density of localized electron states at the Fermi level, and α is the inverse localization length. Using the above equations, a linear plot is expected from $\ln(\rho T^{-1/2})$ *versus* $(1/T)^{1/4}$ for VRH conduction. The linear fit of $\ln(\rho T^{-1/2})$ *versus* $(1/T)^{1/4}$ plot (see inset Fig. 8) indicates that VRH is the dominant mechanism of conduction below a certain temperature T_h. The T_h values are 165 K, 147 K and 140 K for the samples sintered at 600 °C, 800 °C and 1000 °C. The average hopping distance (R) and average hopping energy (E_h) at 150 K have been calculated from $R = [9/8\pi\alpha k_B T N(E_F)]^{1/4}$ and $E_h = 3/[4\pi R^3 N(E_F)]$. Other conditions for VRH conduction[41] are that the value of $\alpha R > 1$ and that $E_h > k_B T$. Both of these conditions are satisfied in all the studied samples (see Table 2). It is not possible that the variation of particle sizes can change the $N(E_F)$, which in effect can account for the large decrease of T_0. However, the decrease of T_0 may indicate the increase of localization length α^{-1} which leads to electronic delocalization.

Ultraviolet-visible spectroscopy

To investigate the optical absorbance and evaluate the optical band gap of $(La_{0.6}Pr_{0.4})_{0.65}Ca_{0.35}MnO_3$, we obtained ultraviolet-visible (UV-Vis) spectra. UV-Vis spectroscopy measurements have been done for $(La_{0.6}Pr_{0.4})_{0.65}Ca_{0.35}MnO_3$ sintered at 600 °C, 800 °C and 1000 °C (Fig. 9). UV-Vis spectra of all the

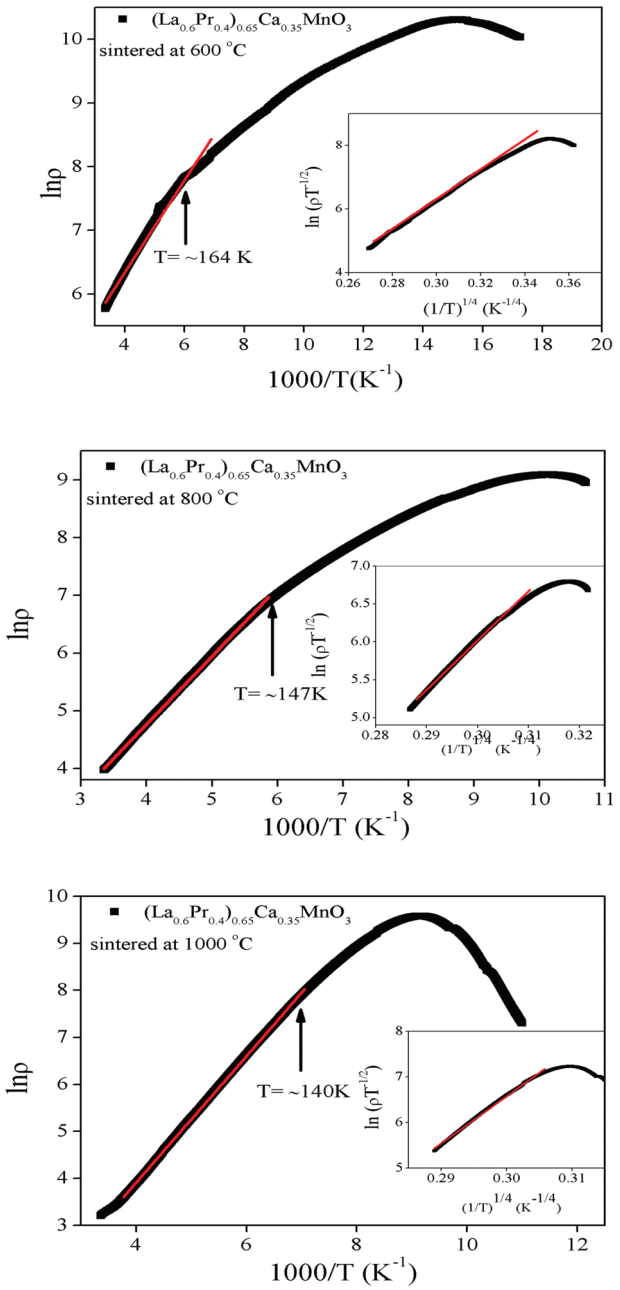

Fig. 8 Variation of $\ln\rho$ as function of 1000/T for $(La_{0.6}Pr_{0.4})_{0.65}Ca_{0.35}MnO_3$ nanoparticles sintered at 600 °C, 800 °C and 1000 °C in low temperature region (for T > 164 K, 147 K and 140 K, respectively). Inset: $\ln(\rho T^{-1/2})$ *vs.* $T^{-1/4}$ in lower temperature region (for T < 164 K, 147 K and 140 K, respectively, and above the metal-semiconductor transition temperature). The linear fit indicates variable range hopping conduction is active in this temperature range.

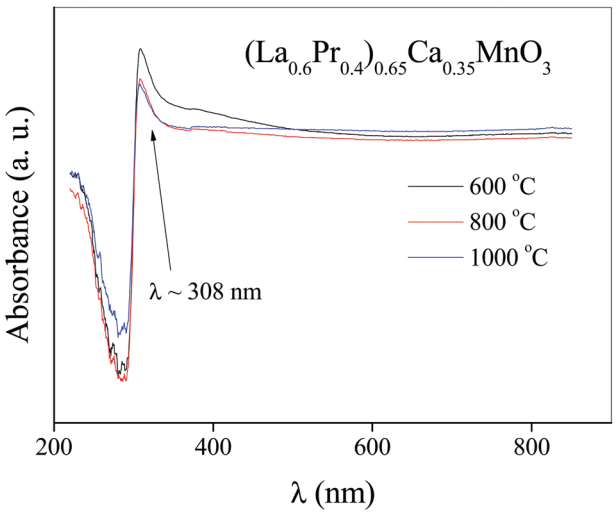

Fig. 9 Ultraviolet-visible spectra of $(La_{0.6}Pr_{0.4})_{0.65}Ca_{0.35}MnO_3$ nanoparticles sintered at 600 °C, 800 °C and 1000 °C.

three samples can be divided into three parts: (i) a sharp absorption edge around 308 nm (ultraviolet region), (ii) an exponential decay region near the absorption edge (ultraviolet to visible region) and (iii) a long smooth extended region (visible to infra-red region). The optical absorption edge has been analyzed as follows:[42]

$$\alpha h\nu \propto \alpha(h\nu - E_g)^n$$

where n is equal to $\frac{1}{2}$ and 2 for direct and indirect transitions, respectively, while absorption coefficient 'α' can be calculated from the following equation:

$$\alpha(\nu) = 2.303 \times (A/d)$$

where 'A' is the optical absorbance, and 'd' is the thickness of the sample. The variations of $(\alpha h\nu)^2$ with photon energy $h\nu$ for $(La_{0.6}Pr_{0.4})_{0.65}Ca_{0.35}MnO_3$ sintered at 600 °C, 800 °C and 1000 °C have been plotted in Fig. 10. $(\alpha h\nu)^2$ varies linearly for a very wide range of photon energy ($h\nu$), which suggests direct type of transitions in these systems. The intercepts of these plots on the energy axis give the energy band gaps of the systems. Direct band gaps of $(La_{0.6}Pr_{0.4})_{0.65}Ca_{0.35}MnO_3$ sintered at 600 °C, 800 °C and 1000 °C determined from these plots are 3.52 eV, 3.46 eV and 3.42 eV, respectively. The decrease in band gap (red-shift) with increasing sintering temperature can be attributed to increased particle sizes, which have been related to the increased metallic behavior in

Table 2 Values of various parameters of variable-range-hopping mechanism of $(La_{0.6}Pr_{0.4})_{0.65}Ca_{0.35}MnO_3$ and activation energy from small polaron theory

Samples	T_0 (K)	α (cm^{-1}) (inverse localization length)	R (cm) (average hopping distance)	Activation energy (eV) (from SPT)	Hopping energy E_h (eV) (from VRH)
$(La_{0.6}Pr_{0.4})_{0.65}Ca_{0.35}MnO_3$ sintered at 600 °C	3.495×10^6	2.918×10^4	7.110×10^{-4}	0.0706	3.37×10^{-6}
$(La_{0.6}Pr_{0.4})_{0.65}Ca_{0.35}MnO_3$ sintered at 800 °C	6.141×10^6	2.815×10^6	1.971×10^{-6}	0.1015	3.80×10^{-4}
$(La_{0.6}Pr_{0.4})_{0.65}Ca_{0.35}MnO_3$ sintered at 1000 °C	1.000×10^7	1.361×10^9	9.919×10^{-8}	0.1146	4.39×10^{-4}

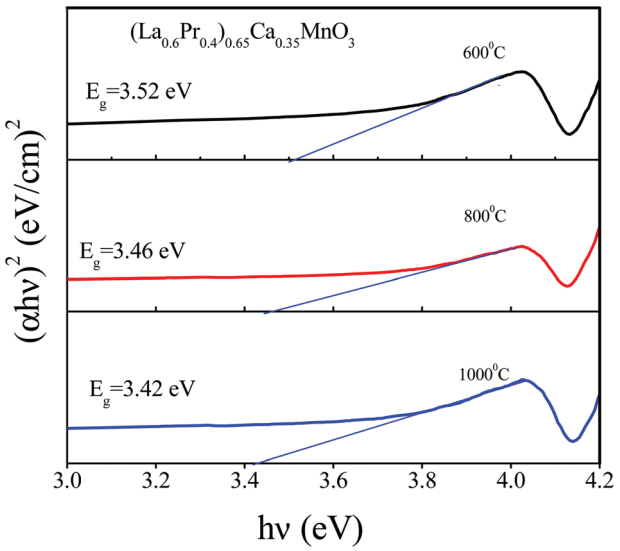

Fig. 10 Variation of $(\alpha h\nu)^2$ *versus* photon energy '$h\nu$' plot for $(La_{0.6}Pr_{0.4})_{0.65}Ca_{0.35}MnO_3$ nanoparticles sintered at 600 °C, 800 °C and 1000 °C.

resistivity analysis. The observed band gaps of these systems appear in the range of wide band gap semiconductors and these values are even more than the band gap of ZnO (3.37 eV) and GaN (3.44 eV).[43–45] In addition, these systems show much better magnetic ordering and magnetic moment[46] than any known diluted magnetic semiconductors, which might prove significant in applications as magnetic semiconductors.

The absorption coefficient near the band edge decays exponentially with photon energy (Fig. 9) and this dependence can be written as follows:[47]

$$\alpha = \alpha_0 \exp\left(\frac{h\nu}{E_u}\right)$$

where 'α_0' is a constant and E_u is Urbach energy, defined as the width of the localized states (related to the amorphous state) present in the forbidden gap. This exponential dependence on photon energy may arise due to the random fluctuations associated with the small structural disorder present within the system.

Conclusion

X-ray diffraction, low-resolution TEM, SAED and X-ray photoemission spectroscopy (XPS) measurements have been done to confirm the phase formation, crystal quality and chemical constituents of our $(La_{0.6}Pr_{0.4})_{0.65}Ca_{0.35}MnO_3$ systems. Crystallite size and grain size calculated from XRD and TEM, respectively, confirm the nano-crystalline structure of our systems. SAED images show that the system becomes more crystalline with increasing sintering temperature. The Raman spectra of $(La_{0.6}Pr_{0.4})_{0.65}Ca_{0.35}MnO_3$ show typical vibration modes of perovskite structures. Raman study confirms the stretching ($B_{2g}(1)$), bending ($B_{2g}(2)$) and tilting ($A_g(2)$) modes of oxygen in MnO_6 octahedra, which play a significant role in structural distortion along with Jahn–Teller distortion ($A_g(1)$) mode, but due to the presence of Pr and Ca in A-site, Jahn–Teller distortion decreases, which is evident from the reduction of $A_g(1)$ mode. FTIR measurements further confirm the presence of characteristic Mn–O stretching vibration mode near 600 cm^{-1}, which is responsible for the structural distortion, magnetic and transport properties of this system. Magnetization measurement shows that the ferromagnetic ordering occurs around 200 K and the system shows a saturation magnetization of 3.43μ_B/Mn, which is very close to the calculated value of the bulk sample. XPS measurement confirms that Mn exists in dual oxidation state (Mn^{3+} and Mn^{4+}), which contributes to double exchange interaction and ferromagnetic ordering. Valence band spectra show two intense peaks around 2.7 eV and 6.2 eV, which is due to strong Mn3d(t_{2g})–O2p hybridization. Resistivity measurement shows that due to the doping of Pr in A-sites, the system started to behave like a charge ordered insulator and insulator-metal transition decreased up to 98 K. With the increase of particle size (by increasing sintering temperature), this insulator-metal transition temperature improves to the higher temperature side. Band gap estimated from UV-Vis measurement appears in the wide band gap semiconductor range (~3.5 eV), which is higher than ZnO (3.37 eV) and GaN (3.44 eV) systems. We believe that with wide band gap and strong magnetic properties, the $(La_{0.6}Pr_{0.4})_{0.65}Ca_{0.35}MnO_3$ system will certainly prove to be a potential candidate for magnetic semiconductor device application.

Acknowledgements

SC is grateful to the funding agencies DST (grant no.: SR/S2/CMP-26/2008), CSIR (grant no.: 03(1142)/09/EMR-II) and BRNS, DAE ((grant no.: 2013/37P/43/BRNS) for financial support. Satyam Kumar is grateful to UGC for financial support. Authors gratefully acknowledge Prof. O. N. Srivastava, Prof. R. S. Tiwari, Prof. P. C. Srivastava and Biophysics lab for their help in providing experimental facilities for TEM, XRD, UV-Vis and FTIR, respectively.

References

1 G. Jonker and J. van Santen, *Physica*, 1950, **16**, 337.
2 E. O. Wollan and W. C. Koehier, *Phys. Rev.*, 1955, **100**, 545.
3 R. von Helmolt, J. Weeker, B. Hopzapfel, L. Schulz and K. Samwer, *Phys. Rev. Lett.*, 1993, **71**, 2331.
4 S. Jin, T. H. Teifel, M. McCormack, R. A. Fastnacht, R. Ramesh and L. H. Chen, *Science*, 1994, **264**, 413.
5 J. Vogier, *Physica*, 1954, **20**, 48.
6 P. Schiffer, A. P. Raniirez, W. Bao and S. W. Cheong, *Phys. Rev. Lett.*, 1995, **75**, 3336.
7 A. P. Ramirez, *J. Phys.: Condens. Matter*, 1997, **9**, 8171.
8 J. M. Coey, M. Viret and S. von Molnar, *Adv. Phys.*, 1999, **48**, 167.

9 M. B. Salamon and M. Jaime, *Rev. Mod. Phys.*, 2001, **73**, 583.
10 E. Dagotto, T. Hotta and A. Moreo, *Phys. Rep.*, 2001, **344**, 1.
11 M. Ziese, *Rep. Prog. Phys.*, 2002, **65**, 143.
12 Z. G. Sheng, M. Nakamura, W. Koshibae, T. Makino, Y. Tokura and M. Kawasaki, *Nat. Commun.*, 2014, **5**, 4584.
13 S. N. Jammalamadaka, J. Vanacken and V. V. Moshchalkov, *Appl. Phys. Lett.*, 2014, **105**, 033505.
14 H. Nakayama, M. Althammer, Y.-T. Chen, K. Uchida, Y. Kajiwara, D. Kikuchi, T. Ohtani, S. Geprägs, M. Opel, S. Takahashi, R. Gross, G. E. W. Bauer, S. T. B. Goennenwein and E. Saitoh, *Phys. Rev. Lett.*, 2013, **110**, 206601.
15 H. Boschker, J. Kautz, E. P. Houwman, W. Siemons, D. H. A. Blank, M. Huijben, G. Koster, A. Vailionis and G. Rijnders, *Phys. Rev. Lett.*, 2012, **109**, 157207.
16 M. Nakamura, Y. Ogimoto, H. Tamaru, M. Izumi and K. Miyano, *Appl. Phys. Lett.*, 2005, **86**, 182504.
17 Y. Ogimoto, N. Takubo, M. Nakamura, H. Tamaru, M. Izumi and K. Miyano, *Appl. Phys. Lett.*, 2005, **86**, 112513.
18 M. Minohara, Y. Furukawa, R. Yasuhara, H. Kumigashira and M. Oshima, *Appl. Phys. Lett.*, 2009, **94**, 242106.
19 C. Zener, *Phys. Rev.*, 1951, **81**, 440.
20 P. W. Anderson and H. Hasegawa, *Phys. Rev.*, 1955, **100**, 675.
21 J. Goodenough, *Phys. Rev.*, 1955, **100**, 564.
22 A. J. Millis, P. B. Littlewood and B. I. Shraiman, *Phys. Rev. Lett.*, 1995, **74**, 5144.
23 A. J. Millis, B. I. Shraiman and R. Mueller, *Phys. Rev. Lett.*, 1996, **77**, 175.
24 A. Gaur and G. D. Varma, *J. Phys.: Condens. Matter*, 2006, **18**, 8837.
25 E. Pollert, S. Krupicka and E. Kuzmicova, *J. Phys. Chem. Solids*, 1982, **43**, 1137.
26 Z. Jirak, S. Krupicka, Z. Somsa, M. Dlouha and S. Vratislav, *J. Magn. Magn. Mater.*, 1985, **53**, 153.
27 Y. Tomioka, A. Asamitsu, H. Kuwahara, Y. Morimoto and Y. Tokura, *Phys. Rev. B: Solid State*, 1996, **53**, R1689.
28 B. Lorenz, A. K. Heilman, Y. S. Wang, Y. Y. Xue, C. W. Chu, G. Zhang and J. P. Franck, *Phys. Rev. B: Condens. Matter*, 2001, **63**, 144405.
29 G. K. Williamson and W. H. Hall, *Acta Metall.*, 1953, **1**, 22.
30 J. Agostinho Moreira, A. Almeida, W. S. Ferreira, J. E. Araújo, A. M. Pereira, M. R. Chaves, J. Kreisel, S. M. F. Vilela and P. B. Tavares, *Phys. Rev. B: Condens. Matter*, 2010, **81**, 054447.
31 V. Dediu, C. Ferdeghini, F. C. Matacotta, P. Nozar and G. Ruani, *Phys. Rev. Lett.*, 2000, **84**, 4489.
32 H. Sakaiand and Y. Tokura, *Appl. Phys. Lett.*, 2008, **92**, 102514.
33 A. Santoni, G. Speranza, M. R. Mancini, F. Padella, L. Petrucci and S. Casadio, *J. Phys.: Condens. Matter*, 1999, **11**, 3387.
34 A. Kowalczyk, J. Baszyński, A. Szajek, A. Ślebarskiand and T. Toliński, *J. Phys.: Condens. Matter*, 2001, **13**, 5519.
35 A. Biswas and I. Das, *Phys. Rev. B: Condens. Matter*, 2006, **74**, 172405.
36 J. van den Brink and D. Khomskii, *Phys. Rev. Lett.*, 1999, **82**, 1016.
37 J. van den Brink, G. Khaliullin and D. Khomskii, *Phys. Rev. Lett.*, 1999, **83**, 5118.
38 N. F. Mott, *J. Non-Cryst. Solids*, 1968, **1**, 1.
39 N. Sharma, S. Granville, S. C. Kashyap and J.-P. Ansermet, *Phys. Rev. B: Condens. Matter*, 2010, **82**, 125211.
40 G. D. Dwivedi, K. F. Tseng, C. L. Chan, P. Shahi, J. Lourembam, B. Chatterjee, A. K. Ghosh, H. D. Yang and S. Chatterjee, *Phys. Rev. B: Condens. Matter*, 2010, **82**, 134428.
41 N. F. Mott and E. A. Davis, *Electronics Process in Non-Crystalline Materials*, Clarendon, Oxford, U.K., 1979.
42 N. F. Mott and R. W. Gurney, *Electronic Processes in Ionic Crystals*, Oxford Univ. Press, London, 1940.
43 A. Mang, K. Reimann and S. Rübenacke, *Solid State Commun.*, 1995, **94**, 251.
44 O. Madelung, *Semiconductors-Basic Data 2nd Revised Edition*, Springer, Berlin, 1996.
45 S. Kumar, S. Chatterjee, K. K. Chattopadhyay and A. K. Ghosh, *J. Phys. Chem. C*, 2012, **116**, 16700.
46 S. Taran, S. Chatterjee and B. K. Chaudhuri, *Phys. Rev. B: Condens. Matter*, 2004, **69**, 184413.
47 F. Urbach, *Phys. Rev.*, 1953, **92**, 1324.